

Boosting Perovskite Solar Cells Efficiency and Stability: Interfacial Passivation of Crosslinked Fullerene Eliminates the “Burn-in” Decay

Changzeng Ding, Li Yin, Jinlong Wang, Valentina Larini, Lianping Zhang, Rong Huang, Mathias Nyman, Liyi Zhao, Chun Zhao, Weishi Li, Qun Luo, Yanbin Shen, Ronald Österbacka, Giulia Grancini,* and Chang-Qi Ma*

Perovskite solar cells (PSCs) longevity is nowadays the bottleneck for their full commercial exploitation. Although lot of research is ongoing, the initial decay of the output power – an effect known as “burn-in” degradation happening in the first 100 h – is still unavoidable, significantly reducing the overall performance (typically of >20%). In this paper, the origin of the “burn-in” degradation in n-i-p type PSCs is demonstrated that is directly related to Li⁺ ions migration coming from the SnO₂ electron transporting layer visualized by time-of-flight secondary ion mass spectrometry (TOF-SIMS) measurements. To block the ion movement, a thin cross-linked [6,6]-phenyl-C61-butyric acid methyl ester layer on top of the SnO₂ layer is introduced, resulting in Li⁺ immobilization. This results in the elimination of the “burn-in” degradation, showing for the first time a zero “burn-in” loss in the performances while boosting device power conversion efficiency to >22% for triple-cation-based PSCs and >24% for formamidinium-based (FAPbI₃) PSCs, proving the general validity of this approach and creating a new framework for the realization of stable PSCs devices.

25.7%.^[1] Though surprising and remarkable progress, PSCs still suffer from unstable power output under the operation blocking their commercial uptake.^[2,3] The instability comes from extrinsic degradation induced by humidity and/or oxygen,^[4] but also from intrinsic deterioration originating from multiple effects such as light-^[5] or bias-^[6] induced decomposition of perovskite layer, thermal-induced phase transition,^[7] electronic field-induced interface reactions or ions migration.^[8–10] While the extrinsic degradation can be avoided to a certain extent by carefully encapsulating the device,^[11–13] the intrinsic degradation paths can be mainly tackled by material, interfaces, and device optimization.^[14–16] Strategies include bulk and surface defect state passivation,^[17–19] interface engineering,^[20,21] and importantly,

1. Introduction

Tremendous progress has been achieved in the field of perovskite photovoltaics in the last 10 years, with certified PCE over


control and inhibition of ion migration.^[9] However, despite a lot of research attention, severe degradation always manifests in the first 100 h of operation, an effect called “burn-in” degradation, limiting the device stability.^[22–24] The “burn-in”

C. Ding, Q. Luo, C.-Q. Ma
School of Nano-Tech and Nano-Bionics
University of Science and Technology of China
398 Jinzhai Road, Hefei 230026, P. R. China
E-mail: cqma2011@sinano.ac.cn

C. Ding, L. Zhang, Q. Luo, R. Österbacka, C.-Q. Ma
i-Lab & Printable Electronics Research Center
Suzhou Institute of Nano-Tec and Nano-Bionics
Chinese Academy of Sciences (CAS)
398 Ruoshui Road, SEID, SIP, Suzhou 215123, P. R. China

L. Yin, C. Zhao
School of Science
School of Advanced Technology
Xi'an Jiaotong-Liverpool University
111 Renai Road, SEID, SIP, Suzhou 215123, P. R. China

J. Wang, W. Li
Shanghai Institute of Organic Chemistry
Chinese Academy of Science
345 Lingling Road, Shanghai 200032, P. R. China

 The ORCID identification number(s) for the author(s) of this article can be found under <https://doi.org/10.1002/adma.202207656>.

V. Larini, G. Grancini
Department of Chemistry & INSTM
University of Pavia
Via T. Taramelli 14, Pavia 27100, Italy
E-mail: giulia.grancini@unipv.it

R. Huang
Vacuum Interconnected Nanotech Workstation
Suzhou Institute of Nano-Tec and Nano-Bionics
Chinese Academy of Sciences (CAS)
398 Ruoshui Road, SEID, SIP, Suzhou 215123, P. R. China

M. Nyman, R. Österbacka
Physics and Center for Functional Materials
Faculty of Science and Technology
Åbo Akademi University
Porthaninkatu 3, Turku 20500, Finland

L. Zhao, Y. Shen
i-Lab
Suzhou Institute of Nano-Tec and Nano-Bionics
Chinese Academy of Sciences (CAS)
398 Ruoshui Road, SEID, SIP, Suzhou 215123, P. R. China

DOI: 10.1002/adma.202207656

degradation significantly reduces the overall power output of the cells (can be as large as 20%) and represents an obstacle in preserving the output efficiency. At present, the precise mechanisms behind such fast degradation are still unknown.^[24]

Previous research work relates “burn-in” degradation to ion migration in the perovskite layer and accumulation at the electron transport layer (ETL)/perovskite interface.^[25,26] Few examples trying to reduce such effect include the work from Nazeeruddin et al. using a guanidinium (Gua)/Cs mixture in $\text{Cs}_x(\text{FAMAGua})_{1-x}$ perovskites to limit the bulk phase segregation and the associated burn-in decay,^[18] the work from Yu et al. using a modified- $\text{PC}_{61}\text{BM}/\text{SnO}_2$ passivating layer forming a more thermodynamically stable charge-transfer complex at the interface, which can inhibit the “burn-in” degradation.^[15] However, such device still suffers of partial initial degradation reducing the output power by 10%. The use of fullerene-based modifiers has been widely explored to push n-i-p PSCs performances.^[27–30] However, the commonly used PC_{61}BM has a high solubility in organic solvents and thus can be easily washed away during deposition perovskite layer, with no control on the resulting layer.^[31,32] In addition, the PC_{61}BM film tends to self-aggregate under illumination or thermal stress, as well as contributing in the delamination of the cell provoking severe instability.^[33]

In this work, we demonstrate the elimination of the “burn-in” degradation in highly efficient n-i-p PSCs by immobilizing the Li^+ ions migration from SnO_2 to the perovskite/hole transporting layer (HTL) interface, which we found being the main cause of it. To suppress it, we introduce a cross-linkable PC_{61}BM (CL- PC_{61}BM) as a functional interlayer in between the SnO_2 and the active perovskite layer. As a result, we demonstrate a push in the device performances reaching 22.16% efficient triple cation-based and 24.19% formamidinium-based perovskite solar cells, with zero losses associated to the “burn-in” degradation, boosting the device stability.

2. Result and Discussion

Interface engineering has been widely explored to enhance the efficiency and stability of PSCs.^[19] In particular, for n-i-p PSCs, defects at SnO_2 surface are responsible for a main decrease in the performance.^[27] To passivate them, fullerene derivatives have been the most popular materials used as surface modifiers.^[34–36] In this work, we used two specific fullerene derivatives to modify the SnO_2 interfaces: [6,6]-phenyl- C_{61} -butyric acid methyl ester (PCBM) and a CL-PCBM film (see Figure 1a for the molecular structures). Figure 1b shows the n-i-p PSCs structure with the PCBM and CL-PCBM films deposited on top of the SnO_2 . The thickness of PCBM and CL-PCBM on SnO_2 before the deposition of perovskite film was measured to be 8.4 and 5.5 nm by atomic force microscope (AFM), as shown in Figure S1 (Supporting Information). Cross-linking of CL-PCBM by thermal annealing was confirmed by the formation of insoluble byproducts, which is consistent with the differential scanning calorimetry results.^[34] To prove the polymerization of CL-PCBM on SnO_2 surface upon thermal annealing at 200 °C, Fourier transform infrared spectroscopy (FTIR) was performed on the CL-PCBM film on CaF_2

before and after thermal annealing. The results are shown in Figure S2 (Supporting Information). Although FTIR signals for C=O and C–O can be clearly identified, the stretching vibration signal for C=C of the acrylate group ($\approx 1600\text{ cm}^{-1}$) is too weak for comparison. To further confirm the success deposition of fullerene layer on SnO_2 , ultraviolet–visible (UV–vis) absorption spectroscopy of the PCBM and CL-PCBM films before and after washing with DMF:DMSO mixed solvent were measured. As shown in Figure S3 (Supporting Information), the absorbance of PCBM film decreased significantly after washing with the solvent, while the CL-PCBM film kept almost the same absorption to its initial value. These results indicate that the CL-PCBM film after thermal annealing showed improved solvent tolerance. In the full device case, the TOF-SIMS analysis (shown in Figure S4, Supporting Information) verifies the formation of a carbon-rich layer on SnO_2 surface. In particular, a more intensive carbon signal is measured for the film with CL-PCBM interlayer with respect to standard PCBM demonstrating that a more condensed CL-PCBM layer formed on SnO_2 upon thermal-induced cross-linking of the fullerene derivatives. The surface morphology of PCBM and CL-PCBM deposited on SnO_2 was also characterized by scanning electron microscope (SEM) and AFM. As shown in Figures S5 and S6 (Supporting Information), the morphology of PCBM film changed after being washed by mixed solvent, whereas the morphology of CL-PCBM showed almost no change upon solvent treatment. The morphology results are in good accordance with the UV–vis and SIMS results, confirming the successful deposition of CL-PCBM on SnO_2 .

Figure 1c,d shows the current density–voltage (J – V) curves of the best triple cations (CsFAMA) and formamidinium (FAPbI₃)-based PSCs upon different J – V sweeping directions, respectively. The J – V curves of the PCBM-based cells are shown in Figure S7 (Supporting Information). The distribution of the device parameters – open circuit voltage (V_{OC}) and fill factor (FF), short circuit current (J_{SC}), as well as the overall PCE are shown in Figure 1e,f. The introduction of the fullerene interfacial layer while partially influencing the J_{SC} (see also the external quantum efficiency (EQE) spectra in Figure S8, Supporting Information), significantly increases the V_{OC} and FF, leading to an overall PCE enhancement of $\approx 10\%$ after surface modification. Note that a slightly increased EQE at 680–750 nm was measured for the cell with CL-PCBM, which ensures a slightly higher J_{SC} for the CL-PCBM-based cell. By checking with the layer thickness of the perovskite film (Figure 2d–f, vide infra), we found that layer thickness of perovskite increases from 400 to 480 nm. This is in good accordance with the UV–vis absorption spectra of these film (Figure S9a, Supporting Information). The numeric simulation revealed that shoulder absorption band shifts from 660 to 720 nm (Figure S9b, Supporting Information), demonstrating that the increase EQE at 700 nm was mainly due to the optical effect originating from the increase of the perovskite thin film. The champion CsFAMA reference cell showed a PCE of 20.19%, with a J_{SC} of 23.39 mA cm^{-2} , a V_{OC} of 1.118 V, and an FF of 77.21%. The use of PCBM and CL-PCBM interfacial layer improves the PCE to 20.51% and 22.16%, respectively, mainly due to the increased V_{OC} (1.140 and 1.178) and FF (77.31% and 79.67%, Figure 1c; Figure S7, Supporting

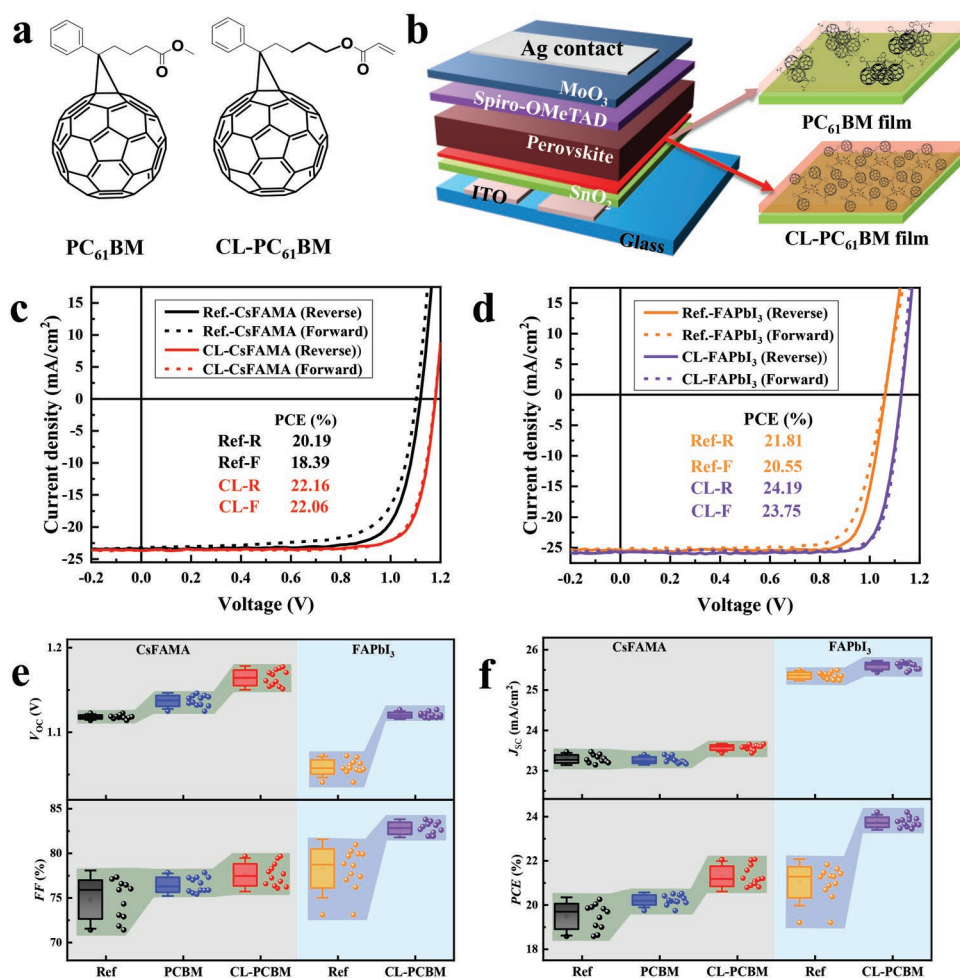


Figure 1. Chemical structure of the fullerene derivatives and the photovoltaic performances of the perovskite solar cells with different interfacial modification layers. a) Chemical structures of PC₆₁BM (PCBM) and cross-linkable PC₆₁BM (CL-PCBM). b) Device structure with the different fullerene passivation thin film between the SnO₂ and perovskite layers. c,d) *J*-*V* curves of the CL-PCBM and reference PSCs based on CsFAMA (c) and FAPbI₃ (excess PbI₂ of 15%) (d) photoactive layers. e,f) Comparison of the statistical *V*_{oc} and FF (e), *J*_{sc}, and PCE (f) of the solar cells with PCBM and CL-PCBM passivation layer to that of the reference cells (note: chemical compositions of the perovskite films are shown in the corresponding figure).

Information). Compared with PCBM, the CL-PCBM-based cells showed higher device performance, suggesting a better surface passivation effect of the CL-PCBM layer, which can be attributed to the more condensed CL-PCBM film on SnO₂ after cross-linking in agreement with the TOF-SIMS analysis (Figure S4, Supporting Information). Similarly, improved *V*_{oc} (1.125 V vs 1.061 V) and FF (83.80% vs 81.41%) yield enhanced the PCE reaching 24.19% (vs 21.81%) for the CL-PCBM-based FAPbI₃ cells (Figure 1d). The photovoltaic performance data are summarized in Table 1. FAPbI₃-based PSCs using aluminum (Al) as the top metal electrode were also fabricated and tested. Figure S10 (Supporting Information) shows the *J*-*V* curves and the statistical photovoltaic performance data of the cells compared to the reference cells. Although the Al-based cells showed lower PCE than the corresponding Ag-based cells (22.39% vs 24.19%), the better surface passivation effect of the CL-PCBM layer can still be confirmed (22.39% vs 20.50%, Figure S10, Supporting Information), confirming the validity of our findings.

To better investigate the origin of such improvement in the device performances, we further characterize the morphology

and the crystal quality of the perovskite layer deposited on top of the modified interface. Figure 2a–c displays the SEM images of CsFAMA perovskite crystals deposited on SnO₂, SnO₂/PCBM, and SnO₂/CL-PCBM, respectively. Nano-sized pinholes (marked in circles) are visible between some grains in perovskite film deposited on SnO₂. On the other hand, the morphology of the perovskite on top of PCBM/CL-PCBM modifications is more compact with no observable pinholes, showing the better quality of perovskite crystals. In addition, the cross-section images of the solar cells with different ETLs, as shown in Figure 2d–f, revealed that pinholes are formed at the SnO₂/perovskite interface, whereas less pinholes were found at the SnO₂/PCBM/perovskite. For the CL-PCBM-modified cell, the pinholes at the interface of SnO₂/CL-PCBM/Perovskite were fully eliminated and a compact interface was formed. Also, the introduction of CL-PCBM layer yield a thicker perovskite film with a thickness of 480 nm. The results indicate that the CL-PCBM modification is beneficial to reduce the defects at the interface of ETL/Perovskite and form a thicker perovskite film. The Dark *J*-*V* curves of the electron-only devices with

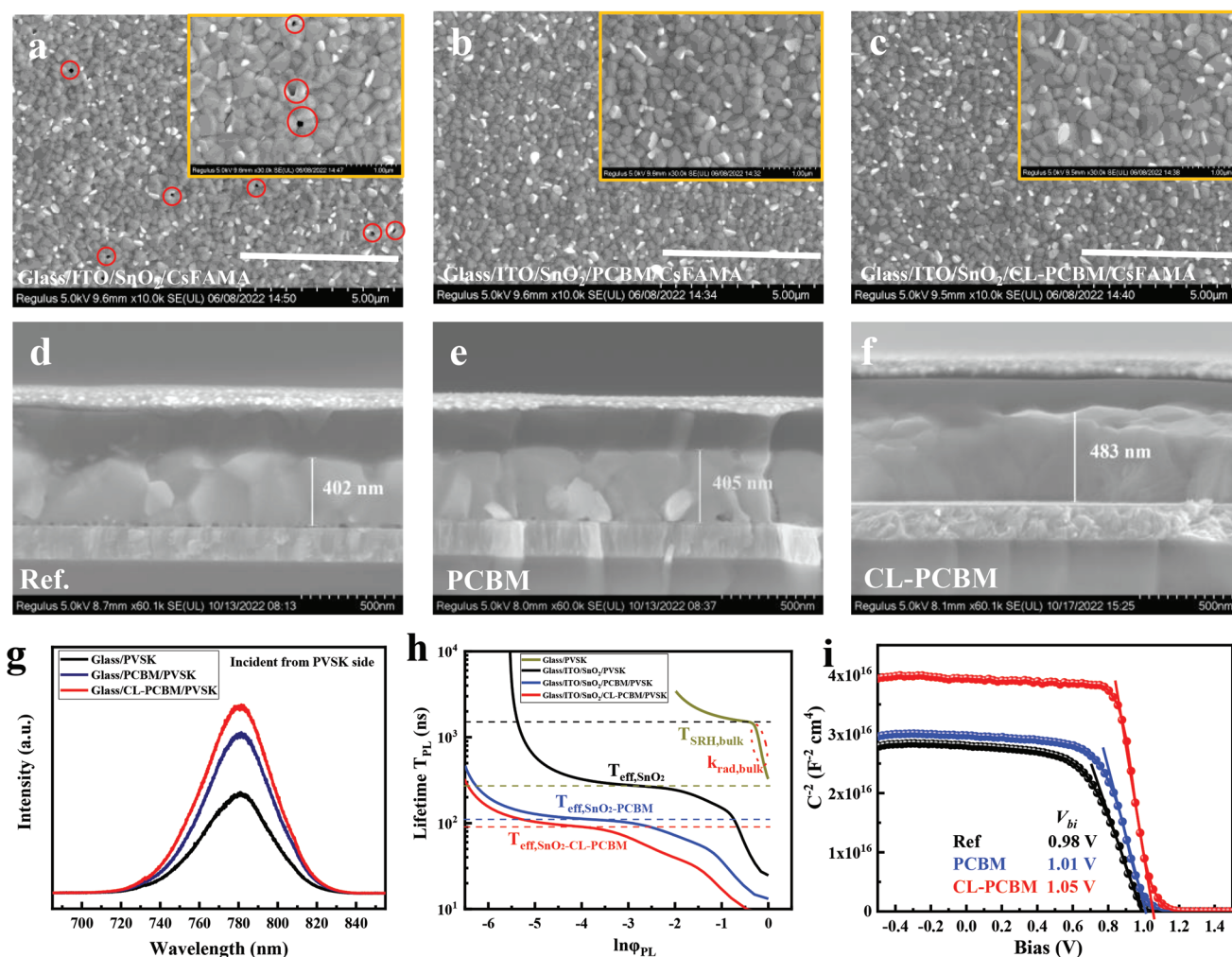


Figure 2. SEM images, Steady state photoluminescence (PL), and Mott–Schottky (M–S) curves based on CsFAMA PSCs with different ETLs. The SEM images of a) SnO₂, b) SnO₂/PCBM, and c) SnO₂/CL-PCBM-based CsFAMA perovskite films. The cross-sectional images of d) Reference, e) PCBM and f) CL-PCBM-modified cells. g) PL spectra of perovskite film deposited on Glass, Glass/PCBM, and Glass/CL-PCBM substrate. h) Differential lifetime as a function of the logarithm of the TRPL intensity, which serves as a relative measure of the quasi-Fermi level splitting, $\ln(\phi_{PL}) \propto \Delta E_F$. The plateau of τ_{PL} seen for the pristine perovskite sample was used to estimate the Shockley Read Hall (SRH) lifetime $\tau_{SRH,bulk}$ in the bulk. i) M–S curves of the reference, PCBM and CL-PCBM-based cells.

and without PCBM/CL-PCBM passivation layer showed a higher injection current at high voltage (Figure S11, Supporting Information), indicating a better interface for the fullerene

incorporated cells. The crystallinity of FAPbI₃ perovskite films deposited on SnO₂ and SnO₂/CL-PCBM substrate was also tested by SEM (Figure S12a,b, Supporting Information), and

Table 1. Photovoltaic performance data of the PSCs deposited on various ETL.

Perovskite	ETL	Scan direction	V _{OC} [V]	J _{SC} [mA cm ⁻²]	FF [%]	PCE [%]
CsFAMA	SnO ₂	Reverse	1.118	23.39	77.21	20.19
		Forward	1.101	23.22	71.92	18.39
	SnO ₂ /CL-PCBM	Reverse	1.178	23.63	79.67	22.16
		Forward	1.176	23.62	79.44	22.06
FAPbI ₃	SnO ₂	Reverse	1.061	25.39	81.41	21.81
		Forward	1.057	25.31	76.80	20.88
	SnO ₂ /CL-PCBM	Reverse	1.125	25.66	83.80	24.19
		Forward	1.124	25.60	82.54	23.75

results show an improved thin film quality of the FAPbI₃ film on CL-PCBM. Knowing that the crystallinity of the perovskite film is sensitive to the surface's wettability, we attribute the improvement in the perovskite film to the hydrophobic property of the fullerene layer. The similar passivation effect of CL-PCBM was also found in dark *J*-*V* curves of electron-only devices, as shown in Figure S12c (Supporting Information).

The steady-state photoluminescence (PL) and time-resolved photoluminescence (TRPL) measurements are then carried out to study the effect of ETLs on crystallinity of the CsFAMA perovskite and the interfacial charge dynamics of ETL/Perovskite. Figure 2g reports the photoluminescence (PL) spectra of the perovskite film deposited on the different surfaces. As seen there, more intensive PL was measured for the perovskite films deposited on Glass/PCBM and Glass/CL-PCBM surfaces, suggesting a less nonradiative recombination within the film with CL-PCBM, which can be ascribed to the increase of the crystalline quality and the improved interface connection (Figure 2a–f), which also indicate the decreased nonradiative recombination in the perovskite layer.

To distinguish the effect of bulk and interface after PCBM/CL-PCBM modification, the TRPL of perovskite film deposited on ITO substrate with different ETLs was characterized, results are shown in Figure S13 (Supporting Information). It has proved that the traditionally used exponent lifetime could not distinguish the effects in bulk and at the interface, a differential lifetime can help to distinguish these effects.^[37,38] The detail of differential lifetime of TRPL results can be found in Supporting Information. In Figure 2h, the plateau of τ_{PL} for the samples with ETL is in this case given by a complex interplay of the bulk SRH lifetime and the surface recombination velocity *S* (Here, we assumed the energy level offset at the interface is negligible). Hence, the surface recombination velocity *S* can be calculated with the following equation and the related results are shown in Table S3 (Supporting Information).

$$\tau_{SRH,eff} = \left(\frac{1}{\tau_{SRH,bulk}} + \frac{S}{2d} \right)^{-1} \quad (1)$$

where *d* is the thickness of the perovskite layer, which can be found in Figure 2d–f. Hence, the CL-PCBM passivation layer could increase *S* from 246 to 975 cm s⁻¹, indicating that the majority carriers will experience a better extraction through that interface.

On the other side, aiming at elucidating the charge transporting/recombination dynamics at the ETL/perovskite interfaces, we performed the Mott–Schottky (*M*-*S*) test on different PSCs. Figure 2i depicts the *M*-*S* diagram of reference, PCBM and CL-PCBM cells. Assuming a uniformly doped in the perovskite layer, and that the highly conductive Spiro-OMeTAD and SnO₂ layers act as extensions of the contacts, the measured capacitance *C* relates to the applied potential *V* as $C^{-2} = 2(V_{bi} - V)/(A^2 q \epsilon \epsilon_0 N_d)$,^[39] where ϵ is the static permittivity (≈ 62 for CsFAMA perovskite material),^[40] ϵ_0 is the permittivity of free space, *A* is the active area of the devices, *q* is the elementary charge, *N_d* is the doping density, and *V_{bi}* is the built-in potential. *V_{bi}* was determined from the intersection of the tangent of the linear part of the Mott–Schottky plots with the *x*-axis. The pristine SnO₂-based PSCs exhibited a *V_{bi}* of

0.98 V, whereas the PCBM- and CL-PCBM-based PSCs exhibited an enhanced *V_{bi}* of 1.01 and 1.05 V. Enhancing the *V_{bi}* has previously been shown to improve device performance, in particular the *V_{OC}*, explaining the *V_{OC}* enhancement obtained.^[41] The perovskite layer is moderately doped with similar doping densities; the *N_d* of three devices can be extracted to be 8.1 × 10¹⁶, 1.1 × 10¹⁷, and 1.8 × 10¹⁷ cm⁻³ for the reference, PCBM- and CL-PCBM-based PSCs, respectively. In FAPbI₃ cells, the *V_{bi}* was also improved from 1.00 to 1.06 V, upon SnO₂ surface modification with CL-PCBM (Figure S12d, Supporting Information), corresponding to an increased *N_d* from 8.45 × 10¹⁶ to 1.44 × 10¹⁷ cm⁻³, again demonstrating the similar surface passivation effect of the CL-PCBM layer. One should note that although the initial layer thicknesses of PCBM and CL-PCBM were ≈ 8.4 and 5.5 nm (vide supra), layer thickness of PCBM should be significantly reduced owing to the solvent washing effect, while CL-PCBM should have a layer thickness ≈ 5 nm for its more robust against solvent (Figure S3, Supporting Information). Assuming the C signal intensity in SIMS is proportional to the layer thickness, the yield PCBM layer is estimated to be 1.1 nm, that is 1/5 of CL-PCBM layer (Figure S4, Supporting Information). Considering the layer thickness of perovskite is ≈ 400 nm, the influence of the layer thickness of PCBM and CL-PCBM on the capacitance of the cells is neglectable. However, a thicker perovskite layer for CL-PCBM-based cell significantly influences the capacitance of the cells, yielding a higher *C*⁻² in Figure 2f.

How the interfacial modification relates to device stability is pivotal to understand. While it is commonly known that n-i-p type PSCs using SnO₂ as ETL and Li-doped Spiro-OMeTAD as hole transport layer (HTL) show excellent photovoltaic performance, they are often affected by severe losses in device stability that poses severe constraints on the device operation in real conditions.^[20,22,42] This is mainly due to shunting paths originating from the formation of conductive filament that originated from the ions migrations in the Spiro-OMeTAD layer.^[43] Inserting buffer layers such as MoO₃ can be a partial solution to that, simultaneously preventing the oxidation of the silver electrode, creating a smooth thin film, and blocking the holes generated in the cells. However, significant “burn-in” performance decay, which means a loss in the performance up to 20% in the first few hours of operation – affects this PSC architecture (Figure 3a), while remaining stable on longer times. A typical *J*-*V* curve of the cell is shown in Figure S14 (Supporting Information). The PCE decay can be fitted by a bi-exponential decay model, from which we retrieve the first decay of 4.6 h and the second one of 155.4 h, see Figure 3a. Clearly, the rapid “burn-in” degradation at the first stage is responsible for this overall severe performance decay. Monitoring more in details the continuous operation over 6000 s, the reference, PCBM and CL-PCBM devices retained 85%, 90%, and 95% of initial PCE (Figure 3b; Figure S15, Supporting Information), respectively. Indicating that the CL-PCBM modification can effectively improve the stability of PSCs. We study the “burn-in” decay process more in detail during the operational stability test in the first few hours, by performing a continuous *J*-*V* scan (see Figure S16, Supporting Information) and again after storing the cell in the dark for 60 s. A reversible “burn-in” decay is observed,^[26] indicating that reversible

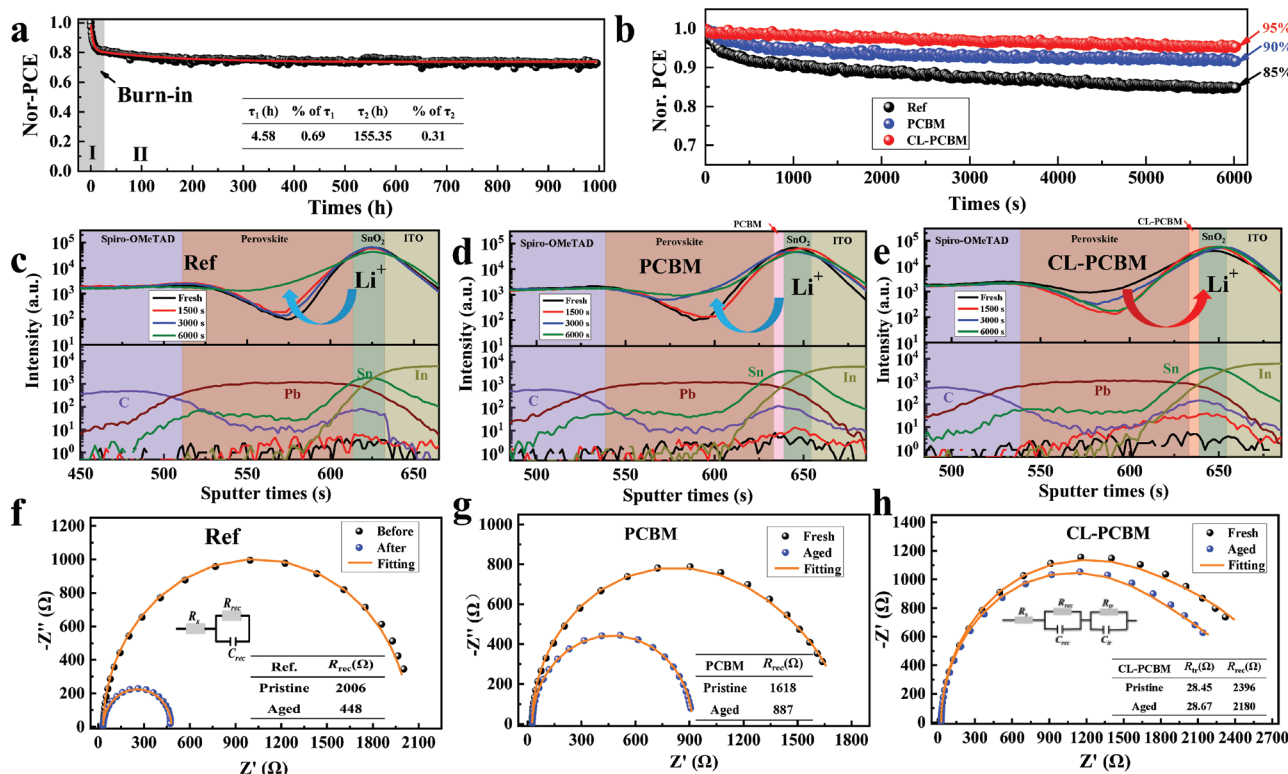


Figure 3. a) The long-term operational stability curves of ref. cells under MPP tracking with continuous illumination. b) Evolution of the PCE of PSCs under continuous light illumination with Li-TFSI-doped Spiro-OMeTAD as HTL and SnO₂, SnO₂/PCBM and SnO₂/CL-PCBM as ETL, respectively. Li⁺ ions profiles and EIS of solar cells. Li⁺ ion profiles test by ToF-SIMS based on c) Reference, d) PCBM and e) CL-PCBM devices. EIS spectrum and fitting results of f) Reference, g) PCBM and h) CL-PCBM devices.

ion migrations are mostly involved in the “burn-in” degradation process (see details in Figure S17, Supporting Information).

To better understand the phenomena behind the “burn-in” degradation, we performed the ToF-SIMS measurement to monitor the depth profiles of the Li⁺ ions soon after *J*-*V* sweeping for different times (see Figure 3c–e). The element distribution profiles for the pristine cells were also measured for comparison. For all these three pristine cells, much higher Li⁺ concentration was measured in the SnO₂ layer than in the Spiro-OMeTAD layer. These findings are similar to our previous report, and the higher Li⁺ concentration in the SnO₂ layer was ascribed to the migration of Li⁺ ions during the deposition and oxidation of Spiro-OMeTAD layer.^[44] In the case of reference cells with bare SnO₂ ETL, diffusion of Li⁺ ions into the perovskite layer happens after a continuous operational stability test, which may change the charge transport and extraction efficiency. Besides Li⁺ ions migration, the I⁻ ions were also easily migrated during the operation of the cells.^[26,45] However, the I⁻ ions profile does not show any changes during the continuous *J*-*V* scanning test, as seen in Figure S18 (Supporting Information), which indicates the migration of I⁻ ions does not cause the “burn-in” degradation process. To further explore this behavior, we measured the electric impedance spectroscopy (EIS) of the cells before and after the operational stability test at *V*_{OC} and in the dark. Figure 3f shows the Nyquist plots and the numerical fitting results according to the equivalent circuit shown in Figure 3f. In the EIS analysis,

the high-frequency component is the signature of the transfer resistance (*R*_{tr}) and the low-frequency is for the recombination resistance (*R*_{rec}).^[46] The *R*_{tr} of the pristine device was found to be rather stable over *J*-*V* sweeping (33.51 Ω vs 32.19 Ω), indicating the electron extraction is not affected upon aging. However, the recombination resistance *R*_{rec} decreased significantly from 2006 to 448 Ω . This means the charge recombination at the interface is increased owing to the accumulation of Li⁺ ions. We then measured the Li⁺ distribution and charge recombination resistance of the PCBM and CL-PCBM modified cells by ToF-SIMS and EIS, respectively. Figure 3d,e,g,h shows the Li⁺ ions distribution and EIS of the PCBM and CL-PCBM-modified devices, respectively. For the PCBM modified device, Li⁺ ions migration from the SnO₂ layer into the perovskite layer was also found. And the *R*_{rec} was decreased from 1618 to 887 Ω for the cell after *J*-*V* sweeping, suggesting the increased charge recombination rate after aging. For the CL-PCBM modified cell, however, decreased Li⁺ ion concentration was measured in the perovskite layer for the cell after age, whereas *R*_{rec} measured from EIS was slightly decreased from 2396 to 2180 Ω . Note that slight “burn-in” degradation was measured for the PCBM-modified cells, while almost no “burn-in” degradation was measured for the CL-PCBM cell (Figure 3b). These results indicate that fullerene derivatives can immobilize Li⁺ within the cell and CL-PCBM exhibits a better immobilization effect. To verify the SnO₂ and PCBM can immobilize Li⁺ ions in the cell, we utilized SnO₂ and PCBM as the cathode for room-temperature

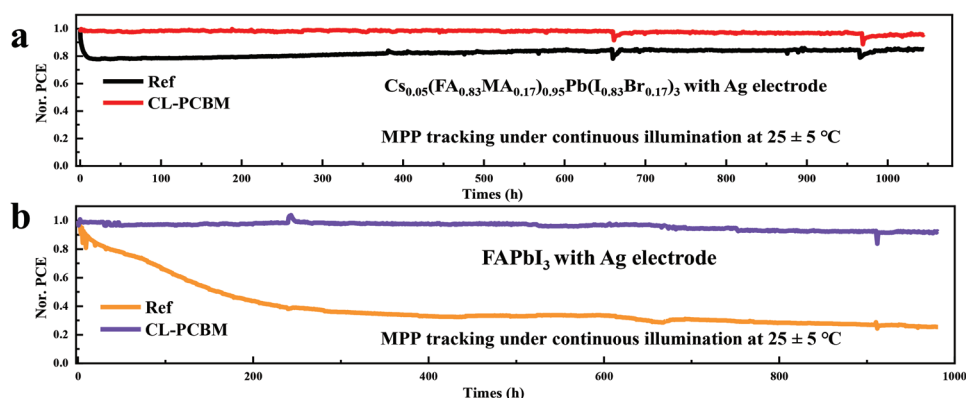


Figure 4. Operational stability of PSCs under MPP tracking with continuous illumination at $25 \pm 5 \text{ }^\circ\text{C}$, a) CsFAMA-based and b) FAPbI₃-based solar cells with Ag top electrode.

Li-ion batteries. The galvanic discharge–charge voltage profiles of both batteries were measured and the results are shown in Figure S19 (Supporting Information). As seen here, both SnO₂ and PCBM have good Li⁺ ions storage capacity during discharge process. However, during the charging process, in Li || SnO₂ cell, the delithiation is more likely to occur, while in Li || PCBM cell, only a small part of Li⁺ ions in PCBM was removed. This indicates that PCBM has excellent capability to immobilize Li⁺ ions. Recently, Qiu et al. reported that owing to the excellent electrochemical reaction of C₆₀, lithiation/delithiation can be formed during the charge–discharge process, and form fullerene–lithium adducts.^[47–49] Since CL-PCBM has similar conjugated molecular core unit as PCBM, the Li⁺ storage mechanism of CL-PCBM should be similar to PCBM. The measured Li⁺ ions migration behavior is in good accordance with the “burn-in” decay of the cells, which indicates Li⁺ ions migration from SnO₂ to the perovskite and spiro-OMeTAD layer is the main reason for the “burn-in” degradation of the cell.

To further confirm that Li⁺ ions migration is involved in the fast “burn-in” degradation, we fabricated n-i-p type perovskite solar cells using P3HT instead of Spiro-OMeTAD layer as the HTL (see Experimental Section and Figures S20–S22, Supporting Information). The Li⁺-doped SnO₂ device using P3HT and HTL manifests the “burn-in” PCE decay ($\approx 20\%$), whereas after depositing a cross-linked CL-PC₆₁BM, the “burn-in” decay process is significantly inhibited. This result strongly confirms that the Li⁺ ions in the SnO₂ layer are a key factor causing the “burn-in” degradation. This is further supported by additional ToF-SIMS (Figure S22b,c, Supporting Information) analysis. For the Li⁺ ions contained devices (device B and C in Figure S20, Supporting Information), Li⁺ ions are found to be mainly located at the perovskite/SnO₂ and perovskite/CL-PCBM/SnO₂ interfaces. The accumulation of Li⁺ ions at the perovskite/P3HT interface was also detected, which can be ascribed to the Li⁺ ion migration from SnO₂:Li⁺ to the HTL. Upon aging, Li⁺ ion concentration at the interface of Perovskite/P3HT increased in device B, in good accordance with the measured “burn-in” decay of device (Figure 3c). Differently, after introducing CL-PCBM, the Li⁺ ions concentration at the perovskite/P3HT interface decreased after aging (Figure S22c, Supporting Information). All these results prove that the

migration of Li⁺ ions from SnO₂ to the interface of perovskite/HTL could be the reason resulting in “burn-in” degradation, whereas the CL-PCBM can immobilize the Li⁺ ions in SnO₂ and consequently minimize the “burn-in” performance degradation. During the operation of the cells, the Li⁺ ions concentrate at the interface of HTL/Perovskite, which increases the charge recombination and decreases the device performance. Although our results showed also the interface connection between SnO₂ and perovskite was improved by introducing a thin fullerene layer, which is beneficial to the stability of the cells, the migration of Li⁺ during the aging is ascribed to the fundamental chemical reason for the “burn-in” degradation according to the results described above.

Finally, the long-term operational stability of PSCs is investigated. Figure 4a shows the PCE evolution of a typical CsFAMA-based PSC with or without CL-PCBM interfacial layer having initial PCE of 19.70% and 22.03%, respectively (see Figures S23 and S24, Supporting Information). As seen here, the reference cell shows a rapid “burn-in” degradation in the first 20 h, which led to an overall 20% PCE decay. After being modified by CL-PCBM, the burn-in degradation was inhibited. The CL-PCBM-based device retains 95% of initial efficiency after aging over 1000 h, demonstrating the simultaneous performance and stability improvement effect of the CL-PCBM layer. Note that the PCBM-based cells showed also “burn-in” decay upon long time aging (Figure S25, Supporting Information), which could be due to the lower layer thickness of PCBM layer owing to the washing effect during the deposition of perovskite layer (vide supra, Figures S3 and S4, Supporting Information).

Similarly, we tested the long-term operational stability of high-performance FAPbI₃-based PSCs with Ag top electrode (see also Figure S26 and statistics in Figure S27, Supporting Information). As shown in Figure 4b, the CL-PCBM layer containing devices showed improved operational stability with zero losses at initial times. After aging for 980 h, the cell with CL-PCBM modification retained the initial PCE of 92%, which are higher than that of the reference cells that decreases for $\approx 25\%$, clearly demonstrating the stabilization effect of CL-PCBM, the statistical stability date is shown in Figure S28 (Supporting Information). Results are also confirmed using Al-based electrodes (Figure S29, Supporting Information).

3. Conclusion

In conclusion, we demonstrated that Li⁺ ions migration from the SnO₂ surface to the perovskite/HTL interface is responsible for the “burn-in” degradation of the n-i-p type of perovskite solar cells. The decreased Li⁺ concentration at the perovskite/SnO₂ interface and the increased Li⁺ concentration at the HTL/perovskite interface simultaneously lower the charge extraction efficiency and increase the charge recombination, and consequently decrease device performance. A thin CL-PCBM forming a uniform surface passivation layer is used to block such movement. As a result, it induces the immobilizing of the Li⁺ ions at the SnO₂ layer reducing charge recombination but it also eliminates the built-in degradation of the cell, synergistically resulting in higher device performance and boosted stability. The current work provides a deep understanding of the “burn-in” degradation process of PSCs, which stems true independently from the composition of the active perovskite layer, providing a new direction for demonstrated efficient and stable solar cells.

4. Experimental Section

Materials: The SnO₂ colloid solution was purchased from Alfa Aesar (tin (IV) oxide, 15 wt.% in H₂O colloidal dispersion). [6,6]-phenyl-C61-butyric acid methyl ester (PC₆₁BM) was purchased from Sigma–Aldrich, crosslink PC₆₁BM (CL-PC₆₁BM) was synthesized by the method in literature.^[34] PbI₂, PbBr₂, CsI, Formamidinium iodide (FAI), methylammonium bromide (MABr), n-Octylammonium iodide (OAI), Lithium bis(trifluoromethanesulfonyl)imide (LiTFSI), Pyridine,4-(1,1-dimethylethyl)- (t-BP) and Spiro-OMeTAD were purchased from Xi’an Polymer Light Technology Corp., dimethylformamide (DMF, purity > 99%), dimethyl sulfoxide (DMSO, purity > 99%), chlorobenzene (CB, purity > 99%), and isopropanol (IPA, purity > 99%) were purchased from J&K scientific. All materials were used directly.

Instruments and Characterization: The *J–V* characters of solar cells were measured with a Keithley 2400 source meter in an N₂ glove box under a simulated sun AM 1.5 G (Newport VeraSol- 2 LED Class AAA Solar Simulator). The EQE of each cell was measured using a home-made IPCE system consisting of a 150 W tungsten halogen lamp (Osram 64 642), a monochromator (Zolix, Omni-I300), an optical chopper, and an *I–V* converter (QE-IV Converter, Suzhou D&R Instruments) equipped with lock-in amplifier (Stanford Research Systems SR 830). To better simulate the device under 1 sun condition, bias light from a 532 nm solid-state laser was introduced to the cell simultaneously. A calibrated Si solar cell was used as a reference. SEM images were gained by a field-emission scanning electron microscope (S-4800) under an accelerating voltage of 5 kV. The time-of-flight secondary ion mass spectrometry (TOF-SIMS 5–100) was measured with the pulsed primary ions from a Cs⁺ (2 keV) liquid-metal ion gun for sputtering and a Bi⁺ pulsed primary ion beam for analysis (30 keV). Electrical impedance spectroscopy (EIS) and Mott–Schottky (M–S) measurements were carried out on the electrochemical workstation (PGSTA302N). The EIS measure conditions were under dark and applied bias at open voltage, the frequency range is 0.1 Hz–10 MHz. The M–S plot measurement conditions were determined to be a 10 kHz frequency.

Preparation of the Solutions: The SnO₂ colloid solution (15 wt.%) was diluted using deionized water to the concentration of 3 wt.%. Then, the solution was stirred at room temperature for 2 h.

PC₆₁BM and CL-PC₆₁BM solution: PC₆₁BM (3 mg) and CL-PC₆₁BM (3 mg) were dissolving in 1 mL CB, stirring at room temperature for 2 h. The Cs_{0.05}(FA_{0.85}MA_{0.15})_{0.95}Pb(I_{0.85}Br_{0.15})₃ (CsFAMA) precursor solution was prepared by dissolving PbI₂ (548.6 mg), PbBr₂ (77.07 mg), FAI (190.12 mg), and MABr (21.84 mg) in a mixture solvent of DMF/DMSO (1 mL, 4:1 v/v). Then, 34 μL CsI (2 m in DMSO)

was added to a mixed perovskite solution, stirring for 2 h at room temperature. The FAPbI₃ precursor solution (1.5 M) was prepared by dissolving PbI₂ 795.24 mg (excess 15%) or 726.09 mg (excess 5%), FAI 257.96 mg, MACI 35 mg and DMACI 3.4 mg in a mixture solvent of DMF/DMSO (1 mL, 4:1 v/v), stirring for 2 h at room temperature. The OAI solution was prepared by dissolving 5 mg OAI into 1 mL IPA, stirring for 2 h at room temperature. The Spiro-OMeTAD solution was prepared by dissolving 72.3 mg Spiro-OMeTAD into 1 mL chlorobenzene followed by the addition of 17.5 μL Li-TFSI (520 mg mL⁻¹ in acetonitrile) and 29 μL t-BP, this solution was stirred overnight at room temperature.

Solar Cell Fabrication: ITO glass was cleaned by ultrasonic cleaning through detergent, and pure water was dried by N₂ gas flow, and cleaned by UV Ozone for 30 min. Then, the substrate was spin-coated with a thin layer of SnO₂ nanoparticle from the SnO₂ colloid solution at 3000 rpm for 30 s, and annealed in ambient air at 150 °C for 30 min. then the SnO₂ film was further treated by UV Ozone for another 10 min. For the PC₆₁BM and CL-PC₆₁BM layer was prepared in N₂ glovebox, 30 μL of PC₆₁BM and CL-PC₆₁BM was dipped on SnO₂ film and spin-coated at 5000 rpm for 30 s, and then annealed at 200 °C for 30 min. The perovskite precursor solution was spin-coated on the SnO₂ and PC₆₁BM/CL-PC₆₁BM substrate.

For the CsFAMA perovskite films, the spin-coated process was divided by a consecutive two-step process, the spin rate of the first step is 2000 rpm for 10 s with an accelerated speed of 500 rpm, and the spin rate of the second step is 6000 rpm for 20 s with an accelerated speed of 1000 rpm. During the second step end of 10 s, 200 μL of ethyl acetate was drop-coated to treat the perovskite films, and then the perovskite films were annealed at 120 °C for 45 min in a glovebox.

For the FAPbI₃, perovskite films were spin-coated at 5000 rpm for 30 s with an accelerated speed of 1000 rpm, during the end of 10 s, 200 μL of chlorobenzene was drop-coated to treat the perovskite films, and then the perovskite films were annealed at 150 °C for 30 min in a glovebox.

After cooling down to room temperature, the OAI solution was coated on perovskite films at 5000 rpm for 30 s. Then, the spiro-OMeTAD solution was coated on perovskite films at 3000 rpm for 30 s with an accelerated speed of 3000 rpm. After that, the Spiro-OMeTAD layer was fully oxidized in the air with a humidity of 30% for 5 h.

After the oxidation process, a fully covered MoO₃ was deposited on spiro-OMeTAD by thermal evaporation with a rate of 0.2 nm s⁻¹, with a thickness of 10 nm. Then, a structured Ag electrode was deposited on the MoO₃ layer with a rate of 0.5 nm s⁻¹, and a thickness of 150 nm. For the Al-based cells, a thickness of 150 nm Al was deposited on MoO₃ with a rate of 2 nm s⁻¹.

Operation Stability Test: Operation stability of the cells was performed on a multi-channel solar cell performance decay testing system ((PVL-G8001M, Suzhou D&R Instruments Co. Ltd.) inside a N₂-filled glove box (H₂O < 10 ppm, O₂ < 10 ppm), and the cells were illuminated with a white LED light (D&R Light, L-W5300KA-150, Suzhou D&R Instruments Co. Ltd.) at a simulated one sun intensity (the initial short current equals to the *J*_{SC} measured under standard condition). The cell’s performance was measured by *I–V* sweeping from 1.2 to –0.05 V, with a step of 0.01 V. The temperature was set at 25 °C. *J–V* characteristics of the cells were measured periodically, and the maximum power output point (mpp) was calculated automatically. An external resistor that matches the mpp point ($R = I_{\text{max}}/V_{\text{max}}$) was then attached to the cells in between *J–V* sweepings according to the *J–V* sweeping results so that the recorded PCE decay curves directly reflect the performance decay of the cells under the simulated operational situation.

Supporting Information

Supporting Information is available from the Wiley Online Library or from the author.

Acknowledgements

The authors would like to acknowledge the financial support from the Chinese Academy of Sciences (No.YJKYYQ20180029), Jiangsu Science

and Technology Program (BE2022021 and BE2022023), Suzhou Science and Technology Program (ST202219), Ministry of Science and Technology Project (G2021014029L), and the “Green flexible hybrid perovskite solar module for the market: from smart lead manipulation to recycling (FLHYPER)” project, funded under the “Circular Economy-2020” call. The authors would also like to thank the technical support for Nano-X from Suzhou Institute of Nano-Tech and Nano-Bionics, Chinese Academy of Science (No. A2107). G.G. acknowledges the “HY-NANO” project that received funding from the European Research Council (ERC) Starting Grant 2018 under the European Union’s Horizon 2020 research and innovation program (grant agreement no. 802862).

Conflict of Interest

The authors declare no conflict of interest.

Data Availability Statement

The data that support the findings of this study are available from the corresponding author upon reasonable request.

Keywords

“burn-in” degradation, cross-linked PCBM, Li⁺ ion migration, operational stability, perovskite solar cells

Received: August 22, 2022

Revised: October 18, 2022

Published online:

- [1] <https://www.nrel.gov/pv/cell-efficiency.html>, (accessed: December 2021).
- [2] K. Domanski, E. A. Alharbi, A. Hagfeldt, M. Grätzel, W. Tress, *Nat. Energy* **2018**, *3*, 61.
- [3] M. V. Khenkin, E. A. Katz, A. Abate, G. Bardizza, J. J. Berry, C. Brabec, F. Brunetti, V. Bulovic, Q. Burlingame, A. Di Carlo, R. Cheacharoen, Y. B. Cheng, A. Colmann, S. Cros, K. Domanski, M. Dusza, C. J. Fell, S. R. Forrest, Y. Galagan, D. Di Girolamo, M. Graetzel, A. Hagfeldt, E. von Hauff, H. Hoppe, J. Kettle, H. Koebler, M. S. Leite, S. Liu, Y. L. Loo, J. M. Luther, et al., *Nat. Energy* **2020**, *5*, 35.
- [4] C. C. Boyd, R. Cheacharoen, T. Leijtens, M. D. McGehee, *Chem. Rev.* **2019**, *119*, 3418.
- [5] Y. Jiang, S.-C. Yang, Q. Jeangros, S. Pisoni, T. Moser, S. Buecheler, A. N. Tiwari, F. Fu, *Joule* **2020**, *4*, 1087.
- [6] M. V. Khenkin, K. M. Anoop, E. A. Katz, I. Visoly-Fisher, *Energy Environ. Sci.* **2019**, *12*, 550.
- [7] J. A. Steele, M. Lai, Y. Zhang, Z. Lin, J. Hofkens, M. B. J. Roeffaers, P. Yang, *Acc Mater. Res.* **2020**, *1*, 3.
- [8] S. Tan, I. Yavuz, N. D. Marco, T. Huang, S.-J. Lee, C. S. Choi, M. Wang, S. Nuryyeva, R. Wang, Y. Zhao, H.-C. Wang, T.-H. Han, B. Dunn, Y. Huang, J.-W. Lee, Y. Yang, *Adv. Mater.* **2020**, *32*, 1906995.
- [9] Y. Zhao, W. Zhou, Z. Han, D. Yu, Q. Zhao, *Phys. Chem. Chem. Phys.* **2021**, *23*, 94.
- [10] S. Ghosh, R. Singh, A. S. Subbiah, P. P. Boix, I. M. Seró, S. K. Sarkar, *Appl. Phys. Lett.* **2020**, *116*, 113502.
- [11] S. Ma, G. Yuan, Y. Zhang, N. Yang, Y. Li, Q. Chen, *Energy Environ. Sci.* **2022**, *15*, 13.
- [12] S. Ma, Y. Bai, H. Wang, H. Zai, J. Wu, L. Li, S. Xiang, N. Liu, L. Liu, C. Zhu, G. Liu, X. Niu, H. Chen, H. Zhou, Y. Li, Q. Chen, *Adv. Energy Mater.* **2020**, *10*, 1902472.
- [13] L. Shi, M. P. Bucknall, T. L. Young, M. Zhang, L. Hu, J. Bing, D. S. Lee, J. Kim, T. Wu, N. Takamura, D. R. McKenzie, S. Huang, M. A. Green, A. W. Y. Ho-Baillie, *Science* **2020**, *368*, 1328.
- [14] Q. Lou, Y. Han, C. Liu, K. Zheng, J. Zhang, X. Chen, Q. Du, C. Chen, Z. Ge, *Adv. Energy Mater.* **2021**, *11*, 2101416.
- [15] P. Hang, J. Xie, C. Kan, B. Li, Y. Zhang, P. Gao, D. Yang, X. Yu, *Adv. Mater.* **2021**, *33*, 2006910.
- [16] F. Zhang, S. Y. Park, C. Yao, H. Lu, S. P. Dunfield, C. Xiao, S. Uličná, X. Zhao, L. D. Hill, X. Chen, X. Wang, L. E. Mundt, K. H. Stone, L. T. Schelhas, G. Teeter, S. Parkin, E. L. Ratcliff, Y.-L. Loo, J. J. Berry, M. C. Beard, Y. Yan, B. W. Larson, K. Zhu, *Science* **2022**, *375*, 71.
- [17] J. Jeong, M. Kim, J. Seo, H. Lu, P. Ahlawat, A. Mishra, Y. Yang, M. A. Hope, F. T. Eickemeyer, M. Kim, Y. J. Yoon, I. W. Choi, B. P. Darwich, S. J. Choi, Y. Jo, J. H. Lee, B. Walker, S. M. Zakeeruddin, L. Emsley, U. Rothlisberger, A. Hagfeldt, D. S. Kim, M. Grätzel, J. Y. Kim, *Nature* **2021**, *592*, 381.
- [18] S. Paek, S. B. Khan, M. Franckevičius, R. Gegevičius, O. A. Syzgantseva, M. A. Syzgantseva, S. Kinch, A. M. Asiri, C. Roldán-Carmona, M. K. Nazeeruddin, *J. Mater. Chem. A* **2021**, *9*, 5374.
- [19] X. Li, W. Zhang, X. Guo, C. Lu, J. Wei, *J. Fang. Sci.* **2022**, *375*, 434.
- [20] Z. Xiong, L. Lan, Y. Wang, C. Lu, S. Qin, S. Chen, L. Zhou, C. Zhu, S. Li, L. Meng, K. Sun, Y. Li, *ACS Energy Lett.* **2021**, *6*, 3824.
- [21] J. Peng, F. Kremer, D. Walter, Y. Wu, Y. Ji, T. Duong, H. Shen, T. Lu, F. Brink, C. Lem, J. Xiang, D. Zhong, L. Li, W. Liu, O. Lee, Y. Liu, K. J. Weber, T. P. White, K. R. Catchpole, *Nature* **2022**, *601*, 573.
- [22] H. Min, D. Y. Lee, J. Kim, M. J. Paik, Y. K. Kim, G. Kim, K. S. Kim, K. S. Lee, J. Kim, M. G. Kim, T. J. Shin, S. I. Seok, *Nature* **2021**, *598*, 444.
- [23] R. Guo, D. Han, W. Chen, L. Dai, K. Ji, Q. Xiong, S. Li, L. K. Reb, M. A. Scheel, S. Pratap, N. Li, S. Yin, T. Xiao, S. Liang, A. L. Oechsle, C. L. Weindl, M. Schwartzkopf, H. Ebert, P. Gao, K. Wang, M. Yuan, N. C. Greenham, S. D. Stranks, S. V. Roth, R. H. Friend, P. Müller-Buschbaum, *Nat. Energy* **2021**, *6*, 977.
- [24] Y.-H. Lin, N. Sakai, P. Da, J. Wu, H. C. Sansom, A. J. Ramadan, S. Mahesh, J. Liu, R. D. J. Oliver, J. Lim, L. Aspirtarte, K. Sharma, P. K. Madhu, A. B. Morales-Vilches, P. K. Nayak, S. Bai, F. Gao, C. R. M. Grovenor, M. B. Johnston, J. G. Labram, J. R. Durrant, J. M. Ball, B. Wenger, B. Stannowski, H. J. Snaith, *Science* **2020**, *369*, 96.
- [25] J. Peng, Y. Wu, W. Ye, D. A. Jacobs, H. Shen, X. Fu, Y. Wan, T. Duong, N. Wu, C. Barugkin, H. T. Nguyen, D. Zhong, J. Li, T. Lu, Y. Liu, M. N. Lockrey, K. J. Weber, K. R. Catchpole, T. P. White, *Energy Environ. Sci.* **2017**, *10*, 1792.
- [26] K. Domanski, B. Roose, T. Matsui, M. Saliba, S.-H. Turren-Cruz, J.-P. Correa-Baena, C. R. Carmona, G. Richardson, J. M. Foster, F. D. Angelis, H. J. M. Ball, A. Petrozza, N. Mine, M. K. Nazeeruddin, W. Tress, M. Grätzel, U. Steiner, A. Hagfeldt, A. Abate, *Energy Environ. Sci.* **2017**, *10*, 604.
- [27] K. Deng, Q. Chen, L. Li, *Adv. Funct. Mater.* **2020**, *30*, 2004209.
- [28] J. Wei, F. Guo, X. Wang, K. Xu, M. Lei, Y. Liang, Y. Zhao, D. Xu, *Adv. Mater.* **2018**, *30*, 1805153.
- [29] S. Zhang, Z. Liu, W. Zhang, Z. Jiang, W. Chen, R. Chen, Y. Huang, Z. Yang, Y. Zhang, L. Han, W. Chen, *Adv. Energy Mater.* **2020**, *10*, 2001610.
- [30] C. Altinkaya, E. Aydin, E. Ugur, F. H. Isikgor, A. S. Subbiah, M. D. Bastiani, J. Liu, A. Babayigit, T. G. Allen, F. Laquai, A. Yildiz, S. D. Wolf, *Adv. Mater.* **2021**, *33*, 2005504.
- [31] B. L. Watson, N. Rolston, K. A. Bush, T. Leijtens, M. D. McGehee, R. H. Dauskardt, *ACS Appl. Mater. Interfaces* **2016**, *8*, 25896.
- [32] K. Wojciechowski, I. Ramirez, T. Gorisse, O. Dautel, R. Dasari, N. Sakai, J. M. Hardigree, S. Song, S. Marder, M. Riede, G. Wantz, H. J. Snaith, *ACS Energy Lett.* **2016**, *1*, 648.
- [33] C. Tian, G. Betancourt-Solis, Z. Nan, K. Liu, K. Lin, J. Lu, L. Xie, L. Echegoyen, Z. Wei, *Sci. Bull.* **2021**, *66*, 339.

- [34] J.-L. Wang, X.-Q. Chen, X. Yao, S.-C. Wu, L.-N. Liu, W.-J. Xiao, H. Wang, J. Li, Z. Lu, W.-S. Li, *Tetrahedron Lett.* **2017**, *58*, 2695.
- [35] Y. Bai, X. Yao, J. Wang, J.-L. Wang, S.-C. Wu, S.-P. Yang, W.-S. Li, *Tetrahedron* **2019**, *75*, 4676.
- [36] K. Liu, C. Tian, Y. Liang, Y. Luo, L. Xie, Z. Wei, *Nano Res.* **2022**, *15*, 7139.
- [37] L. Krückemeier, B. Krogmeier, Z. Liu, U. Rau, T. Kirchartz, *Adv. Energy Mater.* **2021**, *11*, 2003489.
- [38] M. Liu, A. Degterev, S. Dahlström, C. Ahläng, S. Wilken, A. Matuhina, M. Hadadian, M. Markkanen, K. Aitola, A. Kamppinen, J. Deska, O. Mangs, M. Nyman, P. D. Lund, J.-H. Smått, R. Österbacka, P. Vivo, *J. Mater. Chem. A* **2022**, *10*, 11721.
- [39] O. Almora, C. Aranda, E. Mas-Marzá, G. Garcia-Belmonte, *Appl. Phys. Lett.* **2016**, *109*, 173903.
- [40] Y. Liu, J. Sun, Z. Yang, D. Yang, X. Ren, H. Xu, Z. Yang, S. F. Liu, *Adv. Optical Mater.* **2016**, *4*, 1829.
- [41] C. Ahläng, M. Nyman, R. Österbacka, *Phys. Rev. Appl.* **2021**, *16*, 014041.
- [42] Y. Yang, H. Lu, S. Feng, L. Yang, H. Dong, J. Wang, C. Tian, L. Li, H. Lu, J. Jeong, S. M. Zakeeruddin, Y. Liu, M. Grätzel, A. Hagfeldt, *Energy Environ. Sci.* **2021**, *14*, 3447.
- [43] C. Ding, L. Yin, L. Zhang, R. Huang, S. Fan, Q. Luo, J. Lin, F. Li, C. Zhao, R. Österbacka, C.-Q. Ma, *Adv. Funct. Mater.* **2021**, *31*, 2103820.
- [44] C. Ding, R. Huang, C. Ahläng, J. Lin, L. Zhang, D. Zhang, Q. Luo, F. Li, R. Österbacka, C.-Q. Ma, *J. Mater. Chem. A* **2021**, *9*, 7575.
- [45] W. Tress, J. P. C. Baena, M. Saliba, A. Abate, M. Graetzel, *Adv. Energy Mater.* **2016**, *6*, 1600396.
- [46] M. A. Afroz, C. A. Aranda, N. K. Tailor, P. Y. Yukta, M. M. Tavakoli, M. Saliba, S. Satapathi, *ACS Energy Lett.* **2021**, *6*, 3275.
- [47] H. Zhang, S. Zhao, F. Huang, *J. Mater. Chem. A* **2021**, *9*, 27140.
- [48] H. Qiu, J. Wan, J. Zhang, X. Wang, N. Zhang, R. Chen, Y. Xia, L. Huang, H.-L. Wang, *Adv. Sci.* **2021**, *8*, 2101759.
- [49] L. Yin, J. Cho, S. J. Kim, I. Jeon, I. Jeon, M. Park, M. Park, S.-Y. Jeong, D. H. Lee, D.-H. Seo, C.-R. Cho, *Adv. Mater.* **2021**, *33*, 2104763.